High-Speed PM Generator for Optimized Sizing Based on Particle Swarm for Smart Grids

Adel El Shahat, Rami J. Haddad, Youakim Kalaani
Georgia Southern University
aahmed, rhaddad, yalkalaani@georgiasouthern.edu

Abstract

High-Speed, Permanent-Magnet (HSPM) types of micro genearators play an important role in power generation involving Smart Grids Applications. This paper illustrates the benefits of HSPM generators compared to the traditional Permanent Magnet (PM) synchronous machines which offer significant reduction in both weight and volume. An optimized analytical design is proposed and compared with the original machine design of a typical 500 kW output power at tip speed of 250 m/s. These two designs take into consideration multiple factors including classical sizing and problem formulation for optimizing efficiency with bounded constraints. A Particle Swarm Optimization (PSO) algorithm was formulated to optimize efficiency as an objective or fitness function and to minimize machine size as a non-linear function with bounded parameter constraints. Particle swarm algorithms use population based on flocks of birds or insects swarming. The parameter variables used for this type of optimaztion consist of rotor length to diameter ratio, rotor radius, and stack length. It was determined that using the PSO algorithm in HSPMSG sizing is able solve constrained and unconstrained optimization problems. Test results including simulations using PSO Tool in Matlab showed significant improvement in machine design and performance. Furthermore, it was observed that the proposed technique has the advantage of limiting losses at higher frequencies with low weight/volume applications thus improving overall efficiency. Other system parameters such as power factor were also shown to improve as well. Finally, several analytical design problems with waveform variations, harmonics distortion, rotor losses, and effects of poles changing were provided to show the merit of the proposed optimization technique.

Introduction

There has been increased interest in smart and micro-grids conntect systems, especially those dealing with onsite generation [1]. This is largely due to limitation in the use of traditional power plants heavley constrained by economic and environmental regulations [2]. Length-to-diameter is the most important factor defined as the rotor aspect ratio in high-speed applications [3]. Classical and optimum designs of high speed PM alternators are studied for distributed power generation applications [4]. In the case of a high speed PM motor, temperature sensitivity of magnetic materials is an additional factor and Samarium Cobalt is often used to realize higher temperature designs [1-5]. In fact, there have been extensive studies dealing with HSPM design and applications that were conducted and listed in the literature [5-22]

In this paper, an optimized design process is presented as compared to the classical approach of of typical 500 kW output power generator at 250m/s tip speed. These design methods take into consideration multiple factors including classical sizing and problem formulation with the objective of optimizing efficiency with bounded constraints. The optimized set of variables used in this study are rotor length to diameter ratio, rotor radius, and stack length. It was determined that using the PSO algorithm in HSPMSG sizing can be applied to solve both constrained and unconstrained optimization problems. It was also observed that this design approach has the potential to limit losses at high frequency and low weight/volume resulting in higher overall system efficiency. Other parameters like power factor and maximum ampere-torque ratio were also shown to improve as well. Finally, analytical design examples with waveform variations, harmonics distortion, rotor losses, and effects of poles changing were also provided to show the merit of the proposed optimization technique.

Classical Sizing

I. **Power Requirements and Material Selection.** The overall power requirement for the high speed generator is usually within 5-500 kW range. Key factors affecting the structural and thermal design of a permanent magnet machine are the selections of magnet, stator, and rotor materials.

II. **Permanent Magnets.** The sizing and performance of HSPM motors depend on the permanent magnet materials properties [23]. The magnets must be selected to provide the necessary air gap magnetic field and ample coercive force [24]. Fig. 1 shows the characteristics and typical B-H curves for Ferromagnetic materials [31]. Rare earth magnets such as SmCo and NdFeB offer high performance due to greater power density, high Coercivity, high flux densities, and linearity of the demagnetization curves [25]. NdFeB is preferred because it is cheaper and more readily available [26]. NdFeB magnets are selected to be used in the PM generator with the conservatively assumed values.

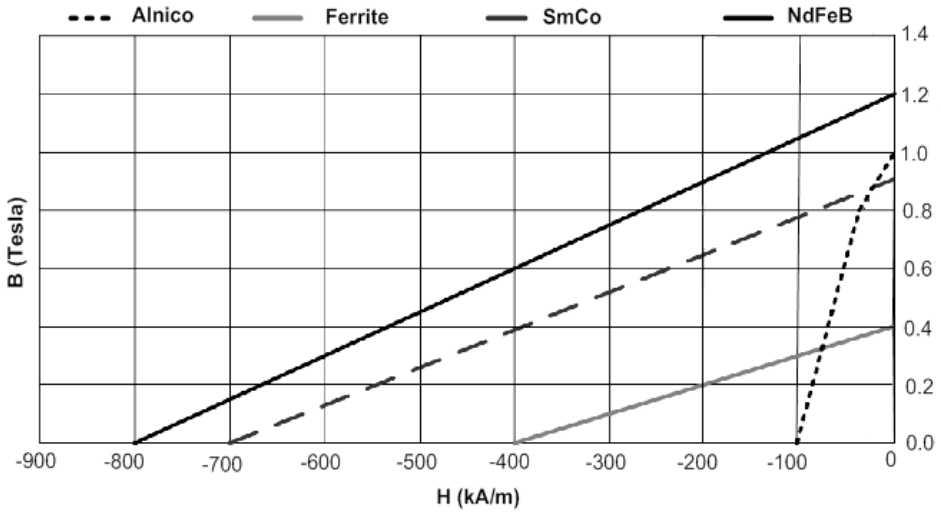

Figure 1: Typical Magnet B-H curves [4], [36]

III. **Stator and Rotor Material.** The rotor is usually built from the same material as the stator for ease of construction but it can be made of any economical steel provided it is strong enough for the given function [31]. The four main materials are low carbon steels, silicon (Si) steels, nickel (Ni) alloy steels, and cobalt (Co) alloy steels [43]. The M19, 29 gauge electrical silicon steel is selected for its economical, thin laminations, and saturation flux density of about 1.8 [31].

Machine Design Parameters

I. **Stator Mechanical Design.** The main aspect considered in this process is the stator mechanical design, either slotted or slotless. A slotless stator has the armature windings located in the air gap of the machine as shown in Fig. 2.

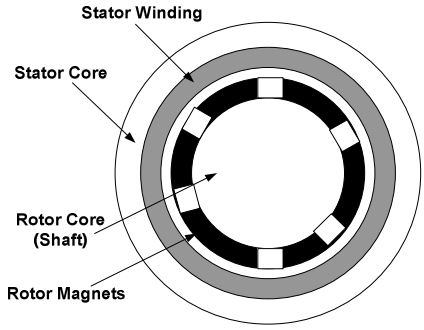

Figure 2: Slotless Stator Design

The overall performance of a slotless stator is always inferior to equivalent slotted stator design and thus, does not appear often in high power applications (Fig. 3). The openings provide rigid housings for the conductors and associated insulation. The stator slot geometry as shown in Fig. 4 is slected to ensure that depression width is the same as the slot top width.

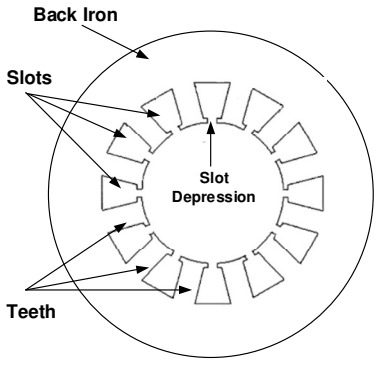

Figure 3: Slotted Stator Design

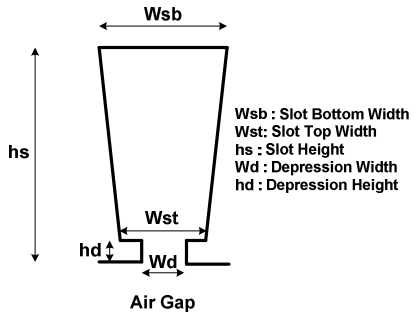

Figure 4: Stator Slot Geometry

In power applications requiring high number of phases, 36 slots are chosen for the initial motor design.

II. **Rotor Mechanical Design.** In high speed applications, the rotor aspect ratio, defined as length to diameter (L/D), is a critical parameter. A normal L/D ratio for wound rotor machine is 0.5 – 1.0 compared to 1 – 3 for a PM machine [27]. The rotor radius and rotational speed also determine the tip speed of the machine which is the surface velocity of the rotor (as defined by Eq. 1).

$$v_{tip} = r\omega_m \tag{1}$$

where ω_m is the angular speed (rad/sec) and r is the rotor radius (m).

For most rotating machines, the upper limit on tip speed is between 100-250 m/s depending on the design criteria [37].

III. **Number of Poles and Magnets Pole Design.** The number of poles in a balanced rotational design is determined by Eq (1) as

$$N(2p) = 120f \tag{2}$$

where N is speed (rpm); p is the number of pole pairs; and f is the electrical frequency (Hz).

For a given rotational speed, an efficient solution is to have large number of poles and higher frequency [31]. The magnet poles are sometimes skewed to reduce cogging torque and smooth out variations in air gap reluctance, flux, and voltage waveforms. A skew factor is shown in Eq. (3).

$$k_{sn} = \frac{\sin(n\theta_s)}{\theta_s / 2} \tag{3}$$

where θ_s is the skew angle (rad) and n is the harmonic number.

IV. **Permanent Magnet Dimensions.** Using a first order approximation, the air gap flux density (B_g) can be represented by Eq. (4) [28].

$$B_g = \frac{h_m}{h_m + g} B_r \tag{4}$$

where h_m is the magnet height (mm); g is the air gap (mm); and B_r is the magnet remnant flux density (T).

In order to get uniform magnetic fields, the magnet height is usually larger than the air gap by a factor of 5 to 10.

V. **Number of phases.** power, current, and voltage ratings in an electric machine is determined by the number of phases Eq. (5).

$$|P + jQ| = q \times V \times I \tag{5}$$

where P is the real power (W); Q is the reactive power (VAR); q is the number of phases; V is the RMS phase voltage (V); and I is the RMS current (A).

VI. Slots per Pole per Phase. The number of slots per pole per phase (m) is an important parameter when considering motor design and it is calculated using Eq. (6).

$$m = \frac{N_s}{2 \times p \times q} \tag{6}$$

where N_s is the number of slots; p is the pole pairs; and q is the number of phases.

VII. Stator Windings. A slot fill factor (λ_s) [31] is used to determine the extend of which the slot cross – sectional area is occupied by winding material Eq. (7).

$$\lambda_s = \frac{Winding\ \ Area}{Total\ \ Slot\ \ Area} \tag{7}$$

Overall, slot fill factors vary in value from 0.3 – 0.7 [31], depending on the number and size of the conductors in the slots. A slot fill factor of 0.5 is assumed.

Machine Calculated Parameters

I. Basic Model. Assuming the machine is balanced, parameters are determined on a per – phase basis and can be applied to all phases as shown in Fig. 5.

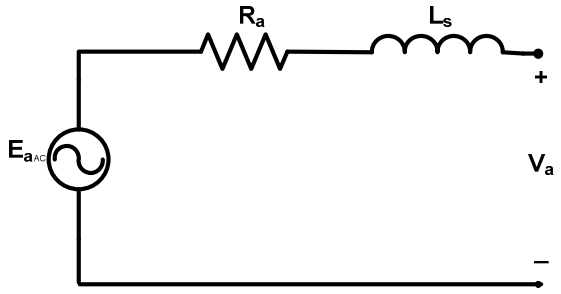

Figure 5: Per Phase Model

II. Winding Resistances. The resistance of the copper phase windings (R_a) is calculated using Eq. (8).

$$R_a = \frac{l}{\sigma \times A} \tag{8}$$

where l is the length of conductor; σ is the winding conductivity; and A is the winding cross – sectional area.

The cross sectional area of the conductor (A_{ac}) is obtained using the slot area and slot fill factor as shown in Eq. (9).

$$A_{ac} = \frac{A_s \times \lambda_s}{2 \times N_c} \tag{9}$$

where A_s is the slot area; and N_c is the number of turns per coil

The power loss resulting from eddy currents in the slot conductors appears as an increased resistance in the winding as in Fig. 6 [36] and determined by Eq (10).

$$P_{ec} = \frac{1}{12}\sigma L \omega_c h^3 \omega^2 \mu_0^2 H_m^2 \tag{10}$$

where H_m is the turn field intensity value; and μ_0 is the permeability of free space.

Since skin depth is defined as

$$\delta s = \sqrt{\frac{2}{\omega \mu_0 \sigma}} \tag{11}$$

Equation (10) can be written as

$$P_{ec} = \frac{L \omega_c h^3}{6\sigma\delta^4} H_m^2 \tag{12}$$

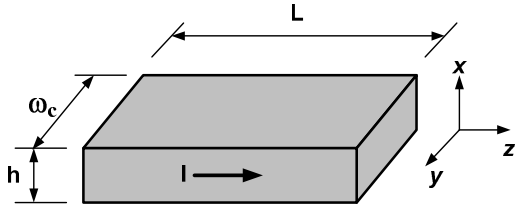

Figure 6: Rectangular Conductor Geometry.

Assuming that the slot conductors are distributed uniformly in the slot, the total slot eddy current loss is calculated by substituting the field intensity into Eq. (12) and summing over all n_s conductors as defined in Eq. (13).

$$P_e = \left(\frac{d_s L h^2 n_s^2}{9\sigma\delta^4 \omega_s} \right) I^2 \tag{13}$$

where I is the RMS conductor current; ω_s is the slot width (m); and d_s is the slot depth (m).

The single slot resistance (R_{sl}) assuming n_s conductors connected in series is:

$$R_{sl} = \frac{\rho n_s^2 L}{k_{cp} \omega_s d_s} \tag{14}$$

where L is the slot length; k_{cp} is the conductor packing factor that is the ratio of cross sectional area occupied by conductors to the entire slot area; and ρ is the electrical resistivity (Ω.m).

Using Eq. (14), the total slot resistance (R_{st}) can be written as

$$R_{st} = R_{sl} + R_{ec} = R_{sl}(1 + \Delta_e) \tag{15}$$

In this equation, $\Delta_e = R_{ec}/R_{sl}$ is a frequency-dependent term. Using Eq. (14) and Eq. (13), this term simplifies to

$$\Delta_e \equiv \frac{R_{ec}}{R_{sl}} = \frac{1}{9}\left(\frac{d_s}{\delta}\right)^2 \left(\frac{h}{\delta}\right)^2 \tag{16}$$

III. Winding and Magnet Factors. A winding factor (k_w) is the ratio of flux linked by an actual winding to the flux linked by a full – pitch, concentrated factor (k_p), and a breadth/distribution factor (k_b) as shown in Eq. (17).

$$k_{wn} = k_{pn} \times k_{bn} \tag{17}$$

The pitch factor can be derived with the final result shown in Eq. (18).

$$k_{pn} = \sin\left(\frac{n \times \alpha}{2}\right) \times \sin\left(\frac{n \times \pi}{2}\right) \tag{18}$$

where n is the harmonic number; and α is the short pitch coil as illustrated in Fig. 7. A phase winding normally consists of numerous coils linking flux slightly out of phase with each other as shown in Fig. 8 .

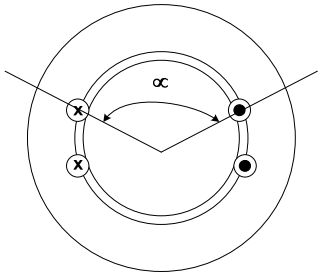

Figure 7: Short – Pitch Coil

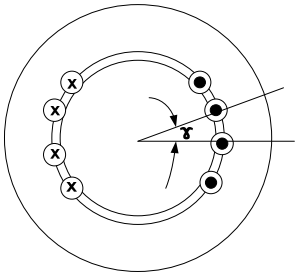

Figure 8: Winding Breadth

The breadth factor is derived either magnetically or geometrically by Eq. (19).

$$k_{bn} = \frac{\sin\left(\frac{n \times m \times \gamma}{2}\right)}{m \times \sin\left(\frac{n \times \gamma}{2}\right)} \tag{19}$$

where m is the number of slots per pole per phase; and γ is the coil electrical angle.
The equation for slotted stator, surface magnet configuration is given by Eq. (20).

$$k_{gn} = \frac{R_i^{\,n_p - 1}}{R_s^{\,2n_p} - R_i^{\,2n_p}} \times \left[\left(\frac{n_p}{n_p + 1} \right) \times \left(R_2^{\,n_p + 1} - R_1^{\,n_p + 1} \right) + \frac{n_p}{n_p - 1} \times R_s^{\,2n_p} \times \left(R_1^{\,1 - n_p} - R_2^{\,1 - n_p} \right) \right] \tag{20}$$

where R_s is the outer magnetic boundary; R_2 is the outer boundary of magnet; R_i is the inner magnetic boundary; R_1 is the inner boundary of magnet;

$$R_s = R + h_m + g\,; \qquad R_i = R_1 = R\,; \qquad R_2 = R + h_m$$

IV. Flux, Voltage and Current. The air gap flux density is also affected by the magnet geometry in the air gap as depicted by Eq. (20). Since the magnet poles rotate north/south, the air gap flux density shape is approximated by Eq (21) as shown in Fig. 9.

$$k_c = \left[1 - \frac{1}{\frac{\tau_s}{w_t} \times \left(5 \times \frac{g}{w_s} + 1 \right)} \right]^{-1} \tag{21}$$

where w_s is the average slot width; w_t is the tooth width; $\tau_s = w_s + w_t$; $w_s = (w_{st} + w_{sb}) / 2$

$$g_e = k_c \times g \tag{22}$$

where g_e is the effective air gap.

$$PC = \frac{h_m}{g_e \times C_\phi} \tag{23}$$

where PC is the permeance coefficient; C_φ is the flux concentration factor (Am/Ag)= $\frac{p \times \theta_m}{180}$

$$B_g = \frac{k_r C_\phi}{1 + k_r \times \frac{\mu_{rec}}{PC}} B_r \tag{24}$$

where μ_{rec} is the recoil permeability; B_r is the remnant flux density (T); and k_r is the reluctance factor

$$B(\theta) = \sum_{\substack{n=1 \\ nodd}}^{\infty} B_n \times \sin(np\theta) \tag{25}$$

$$B_n = \frac{4}{n\pi} \times B_g \times k_{gn} \times \sin\left(\frac{np\theta_m}{2} \right) \times \sin\left(\frac{n\pi}{2} \right)$$

where θ_m is the magnet physical angle.

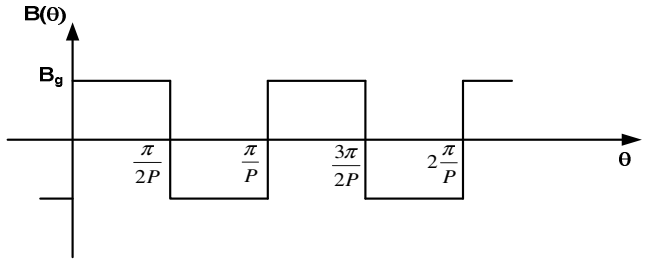

Figure 9: Air Flux Density

Assuming the radial flux through coil (B_{flux}) is sinusoidally distributed, the peak flux (φ_{pk}) for this ideal coil is given by Eq. (27).

$$\phi = \int_0^{\frac{\pi}{P}} B_{flux} \times R_s \times L_{st} d\theta \tag{26}$$

$$\phi_{pk} = \frac{2 \times R_s \times L_{st} \times B_{flux}}{p} \tag{27}$$

Through Faraday's Law, the back EMF (E_a) for the machine is given by Eq. (29).

$$\lambda(\theta) = \sum_{\substack{n=1 \\ nodd}}^{\infty} \lambda_n \times \sin(np\theta) \tag{28}$$

where $$\lambda_n = \frac{2 \times R_s \times L_{st} \times N_a \times B_n \times k_{wn} \times k_{sn}}{p}$$

$$E_a = \sum_{\substack{n=1 \\ nodd}}^{\infty} V_n \times \sin(np\theta) \tag{29}$$

where $$V_n = \frac{d}{dt}\lambda_n = \omega_0 \times \lambda_n$$

The fundamental components are used to determine the internal voltage of the motor as depicted in Eqs. (30) and (31) [4, 36, 37].

$$B_1 = \frac{4}{\pi} \times B_g \times k_g \times \sin\left(\frac{p\theta_m}{2}\right) \tag{30}$$

$$\lambda = \frac{2 \times R_s \times L_{st} \times N_a \times k_w \times k_s \times B_1}{p}$$

$$E_a = \omega_0 \times \lambda \tag{31}$$

The number of armature turns (N_a) could be found using Eq. (32) assuming each slot has 2 half coils.

$$N_a = 2 \times p \times N_c \tag{32}$$

where N_c is the number of turns per coil.

The vector relationship, illustrated in Fig. 10, between terminal voltage (Va), internal voltage (Ea), and the synchronous reactance voltage drop is utilized to obtain Eq. (33) [29].

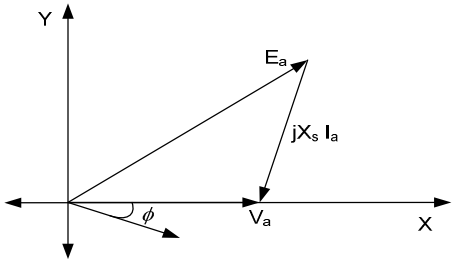

Figure 10: Phasor Relationship

$$V_a = \sqrt{E_a{}^2 + (X_s \times I_a \times \cos\phi)^2} + X_s \times I_a \times \sin\phi \tag{33}$$

$$I_a = \frac{P_{input}}{q \times V_a \times \cos\phi} \tag{34}$$

By substituting Eq. (34) in Eq. (33), (assuming $\cos\phi = 0.99999 \cong 1$) the relation of the voltage could be found as a relation in output power, e.m.f and reactance (which could be calculated using previous and coming sections) from the resulting quadratic equation.

$$V_a^{\,2} = E_a^{\,2} + X_s^{\,2} I_a^{\,2} = E_a^{\,2} + X_s^{\,2} \frac{P_{input}^{\,2}}{9\left(V_a^{\,2}\right)}$$

$$V_a^{\,4} - E_a^{\,2} V_a^{\,2} - X_s^{\,2} \frac{P_{input}^{\,2}}{9} = 0 \quad \text{with} \quad BB = E_a^{\,2}; \qquad CC = X_s^{\,2} P_{input}^{\,2} \big/ 9$$

$$V_a^{\,4} - BB V_a^{\,2} - CC = 0$$

$$V_a = \sqrt{\frac{BB + \sqrt{BB^2 + 4CC}}{2}} \tag{35}$$

The air gap power $P_{air\ gap} = 3E_a I_a = T_e \omega_s = P_{wr} + P_{core} + P_{windage}$ (36)

V. Machine Inductances

To calculate the air gap inductance, a full – pitch, concentrated winding carrying a current I is initially examined which leads to an air gap flux density shown in Eq. (37) [36].

$$B_{flux} = \sum_{\substack{n=1 \\ n\ is\ odd}}^{\infty} B_n \times \sin(np\theta) \tag{37}$$

$$B_n = \frac{4}{n\pi} \times \frac{\mu_0}{(g + h_m)} \times \frac{N_a \times I}{2p}$$

The air gap flux density becomes.

$$B_n = \frac{q}{2} \times \frac{4}{n\pi} \times \frac{\mu_0}{(g + h_m)} \times \frac{N_a \times I}{2p}$$

The flux can be found using Eq. 26 and the total flux linkage is $\lambda = Na\ \phi$. With all real winding effects included, the air gap inductance is then given by Eq. (38).

$$L_{ag} = \frac{\lambda}{i} = \frac{q}{2} \times \frac{4}{n\pi} \times \frac{\mu_0 \times R_s \times L_{st} \times N_a^{\,2} \times k_{wn}^{\,2}}{n^2 \times p^2 \times (g + h_m)} \tag{38}$$

Assuming that the slot is rectangular with slot depressions as illustrated in Fig 4 results in a slot permeance per unit length givewn by Eq. (39) [36], [37].

$$Perm = \frac{1}{3} \times \frac{h_s}{w_{st}} + \frac{h_d}{w_d} \tag{39}$$

Assuming (m) slots per pole per phase and a standard double layer winding, it can be shown that the slot leakage inductance is given by Eq. (40) through Eq. (42).

$$L_{as} = 2 \times p \times L_{st} \times Perm \times [4 \times N_c^{\,2} (m - N_{sp}) + 2 \times N_{sp} \times N_c^{\,2}] \qquad \text{self} \tag{40}$$

$$L_{am} = 2 \times p \times L_{st} \times Perm \times N_{sp} \times N_c^{\,2} \qquad \text{mutual} \tag{41}$$

$$L_{slot} = L_{as} - L_{am} \quad \text{(3 phase)} \quad (42)$$

$$L_{slot} = L_{as} - 2 \times L_{am} \times \cos\left(\frac{2\pi}{q}\right) \quad \text{(higher odd phases)}$$

From [36], the total end turn inductance per phase is defined in Eq. (43).

$$L_e = \frac{\mu_0 \times N_c \times {N_a}^2 \times \tau_s}{2} \times \ln\left(\frac{\tau_s \times \pi}{\sqrt{2 \times A_s}}\right) \quad (43)$$

And the total inductance for the phase is the sum of the three inductances is given by Eq (44).

$$L_s = L_{ag} + L_{slot} + L_e, \qquad X_s = \omega_0 \times L_s \quad (44)$$

Basic Losses

I. Core Losses. Empirical data for M-19, 29 gauge material is obtained. An exponential curve fit is then applied to the data to obtain an equation for estimating the core losses Eq. (45) [31].

$$P_C = P_0 \times \left(\frac{B}{B_0}\right)^{\varepsilon B} \times \left(\frac{f}{f_0}\right)^{\varepsilon f} \quad (45)$$

$$P_{R_c}(\omega) = \frac{V_a^2}{R_c} \quad (46)$$

$$R_c(\omega) = \frac{3\pi^2 {L_{st}}^2 N_a^2 \sqrt{\omega}}{8 c_{Fe} k_{Fe} \left(\frac{1}{\omega_0}\right)^{1.5} \left(\frac{1}{B_0}\right)^2 \left[m_{st} \left(\frac{p\beta_{slot}}{b_{st}}\right)^2 + m_{sy} \left(\frac{1}{h_{sy}}\right)^2 \right]} \quad (47)$$

where R_c is the core resistance, c_{Fe} is the correction factor for iron loss calculation, b_{st} is the stator tooth width, k_{Fe} is the specific iron loss, m_{st} is the stator teeth mass, β_{slot} is the slot angle, and h_{sy} is stator yoke height.

II. Conductor Losses. The conductor losses are then found using the power equation for a resistance Eq. (48).

$$P_{cu} = q \times {I_a}^2 \times R_a \quad (48)$$

III. Friction and Windage Losses. For rotors operating at high speed, friction and windage can cause losses which result in inefficiency and heat production. Friction/windage losses [29] are given by Eq. (49).

$$P_{wind} = C_f \times \pi \times \rho_{air} \times \omega^3 \times r^4 \times L_{st} \quad (49)$$

where C_f is the friction coefficient; ρ_{air} is the density of air. The coefficient of friction can be approximated by Eq. (50).

$$C_f \cong 0.0725 \times R_{ey} - 0.2 \quad (50)$$

where R_{ey} is the Reynold's Number.

Machine Initial Sizing

Air gap magnetic shear stress (τ) is the magnetic shear force developed per unit gap area and is constrained by magnetic design and thermal management [32].

$$\tau \propto K_z B_g \tag{51}$$

where τ is the shear stress (psi); K_z is the surface current density; and B_g is the air gap flux density.

Typical values for air gap shear stress for different types of motors are shown in [32]. For the basic sizing calculations, 10 psi is assumed since the generator is air–cooled and could be at the beginning of liquid–cooled machine area. The fundamental output machine power equation is utilized to derive the rotor radius and stack length of the machine Eq. (52).

$$P_{wr} = 2\pi r L_{st} v_{tip} \tau \tag{52}$$

where r is the rotor radius; L_{st} is the stack length.

The electrical frequency and rotor surface speed are determined as shown in Eq. (53).

$$f = {pN}/{60}, \quad \omega = 2\pi f, \quad \omega = p\omega_m \tag{53}$$

where ω is the electrical frequency (rad/sec); ω_m is the mechanical frequency (rad/sec); and N is the rpm speed.

Machine Detailed Sizing

Once basic sizing is complete, an in-depth analysis is conducted to ascertain the overall performance of the machine within 500 kW power rating. The detailed sizing method is developed using MATLAB. Using the equations presented above, all parameters could be obtained as explained next. Lengths, volumes, and motor mass are calculated using basic geometric equations. A 15% service mass fraction is added to the total mass estimate to account for the additional services associated with machines cooling [32].

I. Rotor variables

h_m = 0.02 [Magnet thickness (m)]; Br = 1.2 [Magnet remnant flux density]; θ_m=50° [Magnet physical angle (deg)]; Magnet skew angle (actual deg) = 10°.

II. Stator variables

q = 3 (number of phases); N_s = 36 (number of slots); N_{sp} = 1 (number of slots short pitched); g = 0.002 [air gap (m)]; t_{frac} = 0.5 (peripheral tooth fraction); h_s = 0.010 [slot depth (m)]; h_d = 0.0004 [slot depression depth (m)]; w_d = 10^{-6} [slot depression width (m)]; s_{yrat} = 0.7 [stator back iron ratio (yoke thick/rotor radius)]; N_c = 1 (turns per coil); λ_s = 0.5 (slot fill fraction); σ_{st} = 6.0×10^7 (stator winding conductivity); and rms = root mean square.

III. Densities

ρ_s = 7700 [steel density (kg/m^3)]; ρ_m = 7400 (Magnet density); ρ_c = 8900 (conductor density).

IV. Constants

$\mu_0 = 4 \times \pi \times 10^{-7}$ (free space permeability); ρ_{air} = 1.205 (density of air at 20°C (kg/m^3))

Magnet Mass: $$M_m = 0.5(p \times \theta_m)\left((r+h_m)^2 - r^2\right)L_{st}\rho_m \quad (54)$$

Tooth width: $$w_t = 2\pi(R+g+h_m+h_d) \times t_{frac} / N_s \quad (55)$$

Slot top width (at air gap): $$w_t = 2\pi(R+g+h_m+h_d) \times (1-t_{frac}) / N_s \quad (56)$$

Slot bottom width: $$w_{sb} = w_{st} \times (R+g+h_s+h_d) / (R+g+h_m+h_d) \quad (57)$$

Stator core back iron depth(as p increases, d_c decreases): $$d_c = s_{yrat} \times R / p \quad (58)$$

Full pitch coil throw: $$N_{sfp} = N_s / (2p) \quad (59)$$

Actual coil throw: $$N_{sct} = N_{sfp} - N_{sp} \quad (60)$$

Estimate end turn length:

End turn travel (one end): $$l_{az} = \pi(R - g + h_m + h_d + 0.5h_s) \times N_{sct} / N_s \quad (61)$$

End length (half coil): $$l_{e_2} = \pi \times l_{az} \quad (62)$$

End length (axial direction): $$l_{e_1} = l_{e_2} / \pi \quad (63)$$

Overall machine length: $$L_{mach} = L_{st} + 2l_{e_1} \quad (64)$$

Core inside radius: $$R_{ci} = R + h_m + g + h_d + h_s \quad (65)$$

Core outside radius: $$R_{co} = R_{ci} + d_c \quad (66)$$

Overall diameter: $$D_{mach} = 2R_{co} \quad (67)$$

Tooth flux density: $$B_t = B_g / t_{frac} \quad (68)$$

Back iron flux density: $$B_b = B_g \times R / (p \times d_c) \quad (69)$$

These set of equations are mainly extracted from references [36], [37] by Hanselmann, Hendershot and Miller.

Particle Swarm Optimization (PSO) Algorithm

A Particle Swarm Optimization (PSO) algorithm is used in this paer and formulated to optimize efficiency as an objective function with bounded parameter constraints. Particle swarm is a population-based algorithm based on flocks of birds or insects swarming. The optimizing variables are rotor length to diameter ratio, rotor radius, and stack length. Simulations were performed using PSO Tool in Matlab. The PSO algorithm could be applied to solve a variety of optimization problems not well-suited for standard optimization techniques in which the objective function is discontinuous, non-differential, stochastic, or highly nonlinear.

HSPM Generator Optimum Efficiency PSO Sizing

The Particle Swarm Optimization (PSO) technique is used [33-35] to optimize the generator efficiency. The optimization variables x_1, x_2, and x_3 are L/D ratio, rotor radius, and rotor stack

length, respectively. the efficiency function, in the form of m-file is implemented. PSO algorithm is then used to maximize the function and generate the desired variables using [1 0 0] constraints as the lower limit, and [3 1 1] as the upper limit. All detailed variables are calculated for the desired high speed permanent magnet synchronous generator. They are used as arguments to generate all basic and detailed variables [36], [37].

$$M_{Total} = M_{Core} + M_{Magnet} + M_{Shaft} + M_{Conductor} + M_{Service} \tag{70}$$

$$M_{Core} = M_{cb} + M_{ct} \tag{71}$$

$$M_{cb} = \rho_s \pi \left(R_{co}^2 - R_{ci}^2\right) L_{st} \tag{72}$$

where M_{cb} is the back iron mass (kg); ρ_s is the steel density (kg/m^3); R_{co} is the core outside radius; and R_{ci} is the core inside radius.

$$R_{ci} = R + h_m + g + h_d + h_s \tag{73}$$

where h_m is the magnet thickness (m); g is the air gap (m); h_d is the slot depression depth (m); and h_s is the slot depth (m).

$$R_{co} = R_{ci} + d_c \tag{74}$$

where d_c is the stator core back iron depth (m).

$$M_{ct} = L_{st} \rho_s \left(N_s w_t h_s + 2\pi R h_d - N_s h_d w_d\right) \tag{75}$$

where M_{ct} is the teeth mass; N_s is the number of slots; w_t is the tooth width; w_d is the slot depression width (m).

$$M_{Magnet} = 0.5\left(p \theta_m \left((r + h_m)^2 - r^2\right) L_{st} \rho_m\right) \tag{76}$$

where θ_m is the magnet physical angle; ρ_m is the magnet density; p is the pole pairs number.

$$M_{Shaft} = \pi R^2 L_{st} \rho_s \tag{77}$$

$$M_{Conductor} = 3 L_{ac} A_{ac} \rho_c \tag{78}$$

where L_{ac} is the armature conductor length; A_{ac} is the armature conductor area (assumes form wound); ρ_c is the conductor density.

$$L_{ac} = 2 N_a \left(L_{st} + 2 l e_2\right) \tag{79}$$

$$A_{ac} = A_s \lambda_s / \left(2 N_c\right) \tag{80}$$

where N_a is the number of armature turns; le_2 is the end length (half coil); A_s is the slot area; λ_s is the slot fill fraction; N_c is the turns per coil.

A 15% service mass fraction is added to the total mass estimate to account for the additional services associated with machines cooling [32].

$$M_{Service} = 0.15\left(M_{Conductor} + M_{Shaft} + M_{Magnet} + M_{Core}\right) \tag{81}$$

$$P_{Total\_Losses} = P_{Core} + P_{Conductor} + P_{Wind} \tag{82}$$

$$P_{input} = P_{Total\_Losses} + P_{out} \tag{83}$$

$$\eta = P_{out} / P_{input} \tag{84}$$

Based on the application, the same techniques could be used to optimize (minimize) the different loss types, mass part of the machine, or any geometric sizing parameter.

Design Comparisons

This section introduces a comparison between the classical and the optimum design procedures. Both design methods were compared at tip speed = 250 m/s and output power of 500 kW. Waveforms of Flux Density Waveform, EMF Waveform, and Harmonic Content are presented. The complete detailed generators parameters for the original and optimized designs are introduced in Table 1 and Table 2, respectively.

Original Design Results

Table 1: Complete Classical Design Parameters

D = 0.0608; L_{st} = 0.1519; rpm = 7.8579e+4; w_t = 0.0046; w_{st} = 0.0046; w_{sb} = 0.0037; d_c = 0.0071; l_{az} = 0.0252; le_2 = 0.0792; le_1 = 0.0252; k_g = 1.1871; w_s = 0.0042; τ_s = 0.0088; g_e = 0.0023; B_g = 0.8583; λ = 0.0736; E_a = 1.2844e+3; L_{ag} = 1.2090e-5; L_{slot} = 5.0754e-6; A_s = 4.1697e-5; L_s = 1.7077e-5; X_s = 0.4216; L_{ac} = 7.4476; A_{ac} = 1.0424e-05; M_{ac} = 2.0729; L_{mach} = 0.2023; R_{ci} = 0.0628; R_{co} = 0.0699; D_{mach} = 0.1397; M_{cb} = 3.4555; M_{ct} = 2.0288; M_c = 5.4843; M_m = 2.3768; M_s = 3.3918; M_{ser} = 1.9989; M_{tot} = 15.3247; R_a = 0.0119; B_t = 1.7166; B_b = 1.2262; P_{cb} = 1.9514e+3; P_{ct} = 2.3382e+3; P_c = 4.2896e+3; V_a = 1.2258e+3; P_{wind} = 2.4655e+3; I_a = 135.9692; P_a = 660.4237; $P_{tlosses}$ = 7.4155e+3; P_{in} = 5.0742e+5; eff = 0.97.
Rotor Losses caused by Harmonics: Time Harmonic Losses = 0.2399 kw; Space Harmonic Losses = 0.0146 kw; Total Rotor Losses = 0.2544 kw; THD = 12.2077 %.

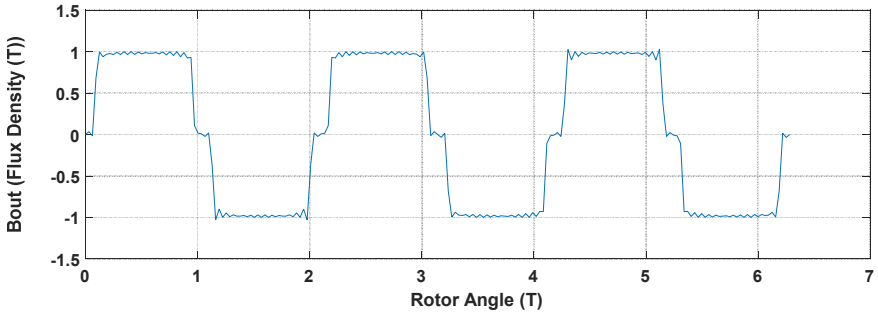

Figure 11: Initial Flux Density Waveform for original design

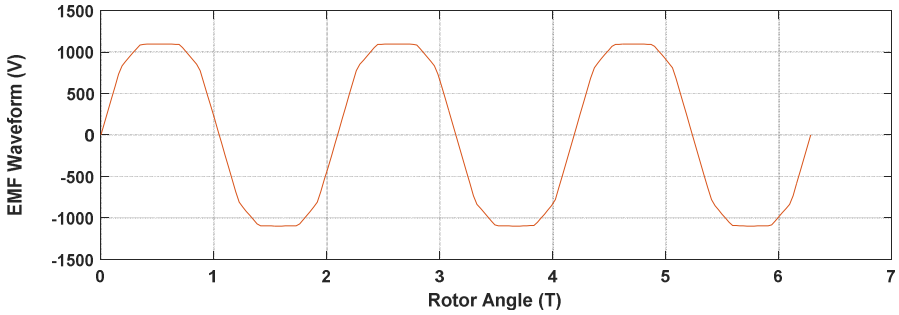

Figure 12: Initial EMF Waveform for original design

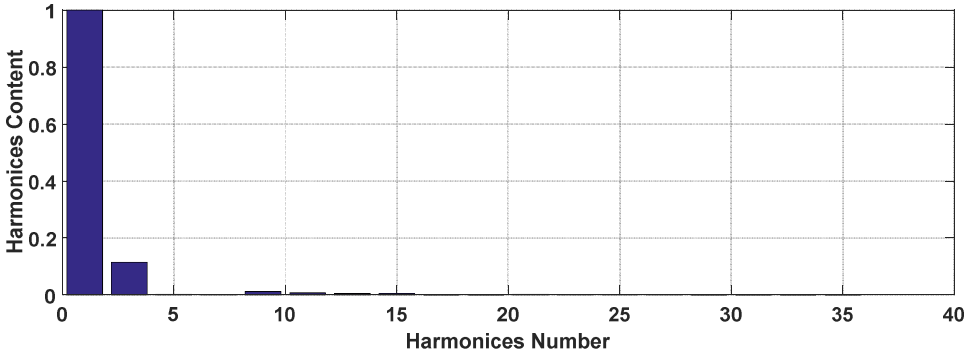

Figure 13: Initial Harmonic Content (12.2077 %) for original design

Efficiency Optimization Results

Efficiency = 0.992; Optimizing variables: x_1 = 1.3943; x_2 = 0.0407; x_3 = 0.1134.

Table 2: Complete Optimized Design Parameters

D = 0.0814; L_{st} = 0.1134; rpm = 5.8683e+4; w_t = 0.0055; w_{st} = 0.0055; w_{sb} = 0.0046; d_c = 0.0095; l_{az} = 0.0297; le_2 = 0.0933; le_1 = 0.0297; k_g = 1.1319; w_s = 0.0051; τ_s = 0.0106; g_e = 0.0024; B_g = 0.8562; λ = 0.0625; E_a = 815.2730; L_{ag} = 1.0805e-5; L_{slot} = 3.1234e-6; A_s = 5.0686e-5; L_s = 1.3898e-5; X_s = 0.2562; L_{ac} = 7.2023; A_{ac} = 1.2671e-5; M_{ac} = 2.4367; L_{mach} = 0.1729; R_{ci} = 0.0731; R_{co} = 0.0826; D_{mach} = 0.1651; M_{cb} = 4.0548; M_{ct} = 1.8204; M_c = 5.8752; M_m = 2.2277; M_s = 4.5417; M_{ser} = 2.2622; M_{tot} = 17.3436; R_a = 0.0095; B_t = 1.7124; B_b = 1.2232; P_{cb} = 1.3949e+3; P_{ct} = 1.2780e+3; P_c = 2.6729e+3; V_a = 756.8998; P_{wind} = 2.4655e+3; I_a = 220.1965; P_a = 1.3780e+3; $P_{tlosses}$ = 6.5163e+3; P_{in} = 5.0652e+5; eff = 0.99; pf = 0.99.
Rotor Losses Caused by Harmonics: Time Harmonic Losses = 0.1675 kw; Space Harmonic Losses = 0.0102 kw; Total Rotor Losses = 0.1776 kw; THD = 11.6276 %.

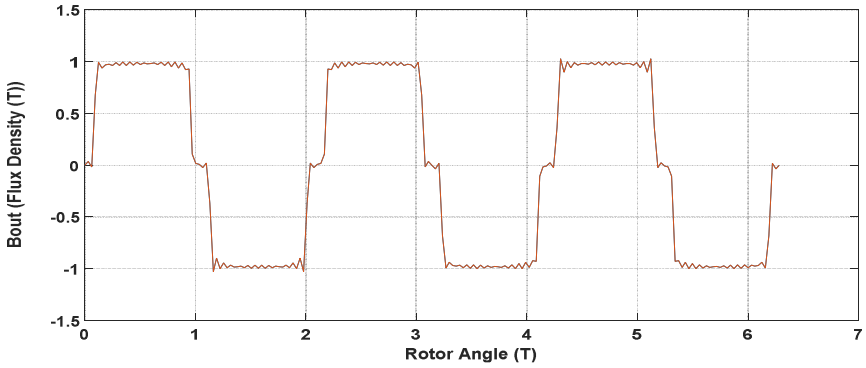

Figure 14: Initial Flux Density Waveform

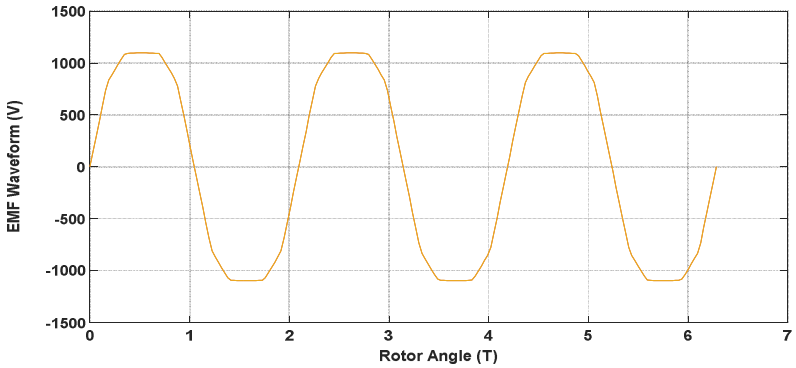

Figure 15: Initial EMF Waveform

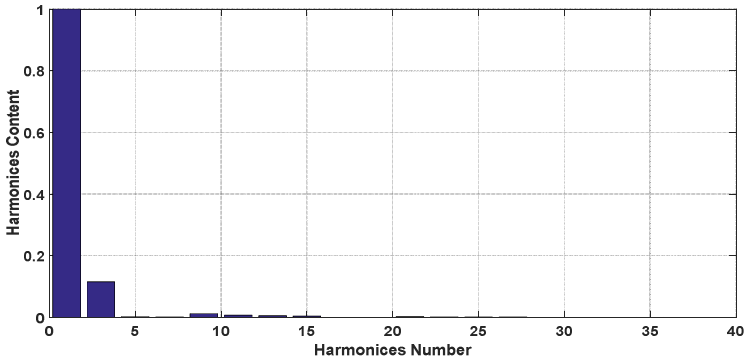

Figure 16: Initial Harmonic Content (11.6276 %)

From waveforms comparisons, it can be seen that THD is improved as a result of reduced lossed and enhanced machine performance

Effect of Number of Poles on Sizing Parameters and M/C characteristics

This section illustrates the effect of the number of poles on parameters and generator characteristics having constant number of slots and phases. Considering the case at 50 kW output power with various tip speeds of 250, 200, 150, and 100m/s. The tested number of poles were 4, 6, and 12. As expected, the number of poles affects the electrical, magnetic, and

structural performance, including frequency, voltage waveforms, magnetic flux, magnetic volume, air gap, and the stator back iron thickness.

In general, if rotational speed is held constant as the number of poles is increased:

- Number of slots/pole/phase changes affecting the output waveforms and THD.
- Deacrease in the weight of the machine.
- Increase in the electrical frequency.

The following figures (17, 18, 19) depict these various effects at 50 kW:

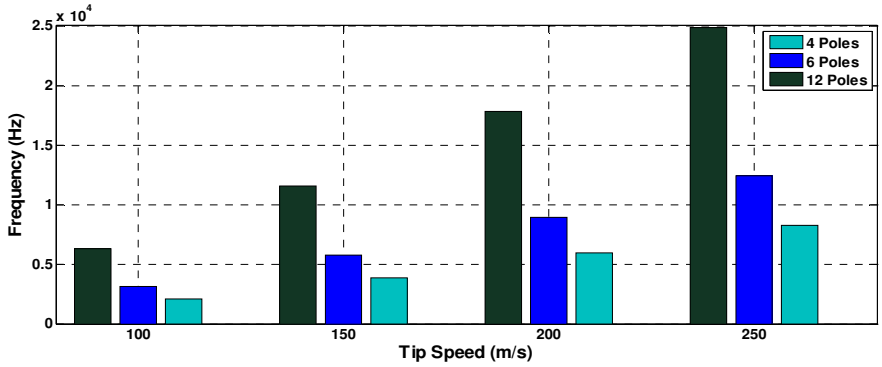

Figure 17: Frequency with Tip Speed for Various Pole Number.

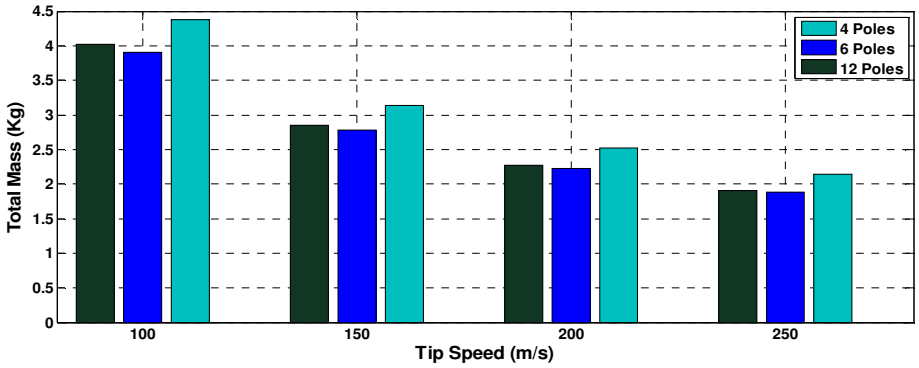

Figure 18: Total Mass with Tip Speed for Various Pole Number.

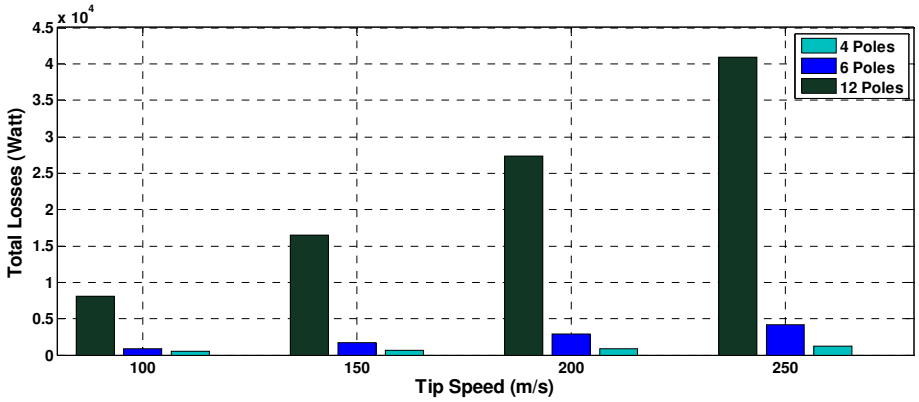

Figure 19: Total Losses with Tip Speed for Various Pole Number.

Based on Fig. 17-19, it is clear that 1) the rpm speed is constant at each tip speed value because the frequency is changed with changing poles number; 2) the frequency is directly proportional with the number of poles at each tip speed; and 3) the magnet mass increases with the number of poles for a specific tip speed and total losses.

Conclusion

This paper provided an elaborate and detailed design analysis for a high speed PM generator as compared to traditional methods. Significant reductions in both weights and volumes were realized for a case study involving a 500 kW, 250m/s machine based on previous work found in the literature. The optimizing variables considered in this study were rotor length to diameter ratio, rotor radius, and stack length with the objective to maximize efficiency. It was determined that using the proposed PSO algorithim in HSPMSG sizing resulted in reduced losses and siginificant improvement in the performance of the machine parameters. Furthermore, it was found that if the rotational speed was held constant as the number of poles increased, the weight of the machine can be decreased and he electrical frequency increased. These design factors can also have an impact on the number of slots/pole/phase affecting THD and the output waveforms of the HSPM generator used in smart-grid applications.

References

[1] Keyhani, A., Marwali, M. N., Dai, M. (2010). *Integration of Green and Renewable Energy in Electric Power Systems*. Wiley.

[2] Keyhani, A. (2009). Cyber-Controlled Smart Microgrid Systems of the Future: The High Penetration of Renewable and Green Energy Sources. *New Research Directions for Future Cyber-Physical Energy Systems Proceedings*, Baltimore, Maryland.

[3] El Shahat, A., Keyhani, A. (2012). Sizing High Speed Micro Generators for Smart Grid Systems. *Smart power Grids 2011, Series: Power Systems*. Springer-Verlag Berlin Heidelberg, 177–234.

[4] El Shahat, A. (2012). PM Synchronous Machine New Aspects; Modeling, control, and design. *LAP Lambert Academic Publishing*.

[5] Ahmad, R. A., Pan, Z., Saban, D. M. (2007). On-Board Electrical Network Topology Using High Speed Permanent Magnet Generators. *IEEE Electric Ship Technologies Symposium*, 7, 356 – 362.

[6] Scridon, S., Boldea, I., Tutelea, Blaabjerg, L., F., Ritchie, E., (2004). BEGA – A Biaxial Excitation Generator for Automobiles: Comprehensive Characterization and Test Results. *39th IEEE IAS Annual Meeting Conference*, 3, 1682 – 1690.

[7] Binder, A., Schneider, T., Klohr, M., (2006). Fixation of Buried and Surface-Mounted Magnets in High-Speed Permanent-Magnet Synchronous Machines. *IEEE Trans. on Industry Applications*, 42, 1031 – 1037.

[8] Hosseini, S. M., Mirsalim, M. A., Mirzaei, M. (2008). Design, Prototyping, and Analysis of a Low Cost Axial-Flux Coreless Permanent-Magnet Generator. *IEEE Trans. on Magnet.*, 44, 75 – 80.

[9] Mellor, P. H., Burrow, S.G., Sawata, T., Holme, M. (2005). A Wide – Speed – Range Hybrid Variable – Reluctance / Permanent – Magnet Generator for Future Embedded Aircraft Generation Systems. *IEEE Trans. on Industry Applications*, 41, 551 – 556.

[10] Sadeghierad, M., Lesani, H., Monsef, H., Darabi, A. (2007). Design considerations of High Speed Axial Flux permanent magnet Generator with Coreless Stator. *The 8th International Power Engineering Conference (IPEC)*, 1098 – 1102.

[11] Arnold, D. P., Das, S., Park, J. W., Zana, I., Lang, J. H., Allen, M. G. (2006). Micro fabricated High-Speed Axial-Flux Multi watt Permanent- Magnet Generators—Part II: Design, Fabrication, and Testing. *Journal of Micro Electromechanical Systems*, 5, 1351 – 1363.

[12] Binder, A., Schneider, T., Klohr, M. (2006). Fixation of Buried and Surface-Mounted Magnets in High-Speed Permanent - Magnet Synchronous Machines. *IEEE Trans. on Industry Applications*, 42, 1031 – 1037.

[13] Paulides, J. J. H., G. Jewell, W., Howe, D. (2004). An Evaluation of Alternative Stator Lamination Materials for a High – Speed, 1.5 MW, Permanent Magnet Generator. *IEEE Trans. on Magnetics*, 40, 2041 - 2043.

[14] El – Hasan, T. S., Luk, P. C. K., Bhinder, F. S., Ebaid, M. S. (2000). Modular Design of High – Speed Permanent – Magnet Axial – Flux Generators. *IEEE Trans. on Magnetics*, 36, 3558 – 3561

[15] Jang, S. M., Cho, H. W., Jeong,Y. H. (2006). Influence on the rectifiers of rotor losses in high – speed permanent magnet synchronous alternator. *Journal of Applied Physics*, American Institute of Physics, 08R315-3.

[16] Hwang, C. C., Tien, C. L., Chang, H. C. (2007). Performance and applications of a small PM generator. *phys. stat. sol.,* 4, 4635 – 4638.

[17] Kolondzovski, Z. (2008). Determination of critical thermal operations for High – speed permanent magnet electrical machines. *The International Journal for Computation and Mathematics in Electrical and Electronic Engineering*, 27, 720-727.

[18] Sahin, F., Vandenput, A.J.A. (2003). Thermal modeling and testing of a High – speed axial – flux permanent – magnet machine. *The International Journal for Computation and Mathematics in Electrical and Electronic Eng.*, 22, 982 – 997.

[19] Vandenput, A.J.A., Sahin, F. (2008). Design considerations of the flywheel-mounted axial-flux permanent-magnet machine for a hybrid electric vehicle. *8th European Conference on Power Electronics and Applications*.

[20] Nagorny, A. S., Dravid, N. V., Dravid, R. H., Kenny, B. H. (2005). Design Aspects of a High Speed Permanent Magnet Synchronous Motor/Generator for Flywheel Applications. *International Electric Machines and Drives Conference*, San Antonio, Texas.

[21] Caricchi, F., Crescimbini, F., Mezzetti, F., Santini, E., (1996). Multistage axial flux PM machine for wheel direct drive. *IEEE Trans. on Industry Applications*, 32, 882—887.

[22] Binns K.J., Shimmin, D.W. (1996). Relationship between rated torque and size of permanent magnet machines. *IEE Proc. Electr. Power Appl.*, 143, 417—422.

[23] Fengxiang,W., Wenpeng, Z., Ming, Z., Baoguo, W. (2002). Design considerations of high speed PM generators for micro turbines. *IEEE trans. energy conversion*.

[24] Pavlik, D., Garg, V., Repp, J., Weiss, J. (1988). A finite element technique for calculating the magnet sizes and inductances of permanent magnet machines. *IEEE trans. of energy conversion*, 3.

[25] Kang, D., Curiac, P., Jung, Y., Jung, S. (2003). Prospects for magnetization of large PM rotors: conclusions from a development case study. *IEEE trans. on Energy Conversion*, 18, 3.

[26] *Website for Magnetic Component Engineering. Inc., 2004.*

[27] Bianchi, N., Lorenzoni, A. (1996). Permanent magnet generators for wind power industry: an overall comparison with traditional generators", *Opportunities and advances in international power generation conference*, 419.

[28] Rahman, M. A., Slemon, G. R. (1985). Promising Applications of Neodymium Iron Boron Iron Magnets in Electrical Machines. *IEEE Trans. On Magnetics*, 5.

[29] Rucker, J. E., Kirtley, J. L., McCoy, Jr. T. J. (2005). Design and Analysis of a Permanent Magnet Generator for Naval Applications. *IEEE Electric Ship Technologies Symposium*, 451 – 458.

[30] Abu Sharkh, S.M., Harris, M. R., Taghizadeh Irenji, N. (1997). Calculation of Rotor Eddy Current Loss in High Speed PM Alternators. *IEE Conference Publication* No. 444.

[31] Polinder, H., Hoeijmakers, M. J. (1999). Eddy – Current Losses in the Segmented Surface Mounted Magnets of a PM Machine. *IEE Proceedings, Electrical Power Applications*, 146, 3.

[32] Pepi, J., Mongeau, P. (2004). High power density permanent magnet generators. *DRS Electric power technologies*, Inc.

[33] Kennedy, J., Eberhart, R. (1995). Particle swarm optimization. *Proc. IEEE International Conf. on Neural Networks,* Perth, Australia.

[34] Clerc, M. (2004). Discrete Particle Swarm Optimization. *New Optimization Techniques in Engineering Springer-Verlag*.

[35] Yasuda, K., Ide, A., Iwasaki, N. (2003). Adaptive particle swarm optimization. *Proceedings of IEEE International Conference on Systems, Man and Cybernetics*, 1554-1559.

[36] Hanselmann, D. C. (1994). Brushless Permanent Magnet Motor Design. *New York: McGraw-Hill*.
[37] Hendershot J. R., Miller, T. J. E. (1994). Design of Brushless Permanent Magnet Motors. *Oxford, U.K.: Magna Physics Publishing and Clarendon Press*.
[36] Hanselmann, D. C. (1994). Brushless Permanent Magnet Motor Design. *New York: McGraw-Hill*.
[37] Hendershot J. R., Miller, T. J. E. (1994). Design of Brushless Permanent Magnet Motors. *Oxford, U.K.: Magna Physics Publishing and Clarendon Press*.

Biographies

ADEL EL SHAHAT is currently an Assistant Professor, Electrical Engineering in the Department of Electrical Engineering at Georgia Southern University. He received his B.Sc. in Electrical Engineering from Zagazig University, Zagazig, Egypt, in 1999. He received his M.Sc. in Electrical Engineering (Power & Machines) from Zagazig University, Zagazig, Egypt in 2004. He received his Ph.D. degree (Joint Supervision) from Zagazig University, Zagazig, Egypt, and The Ohio State University (OSU), Columbus, OH, USA, in 2011. His research focuses on various aspects of Power Systems, Smart Grid Systems, Power Electronics, Electric Machines, Renewable Energy Systems, Energy Storage, and Engineering Education. Dr. El Shahat may be reached at aahmed@georgiasouthern.edu

RAMI J. HADDAD is currently an Assistant Professor in the Department of Electrical Engineering at Georgia Southern University. He received his B.S. degree in Electronics and Telecommunication Engineering from the Applied Sciences University, Amman, Jordan, his M.S. degree in Electrical and Computer Engineering from the University of Minnesota, Duluth, MN, and his Ph.D. degree from the University of Akron, Akron, OH. He is an IEEE senior member. His research focuses on various aspects of optical fiber communication/networks, broadband networks, multimedia communications, multimedia bandwidth forecasting and engineering education. Dr. Haddad may be reached at rhaddad@georgiasouthern.edu.

YOUAKIM KALAANI is an Associate Professor of Electrical Engineering in the Department of Electrical Engineering at Georgia Southern University. Dr. Kalaani received his B.S. degree in Electrical Engineering from Cleveland State University (CSU). He graduated from CSU with M.S. and Doctoral degrees in Electrical Engineering with concentration in power systems. Dr. Kalaani is a licensed professional engineer (PE) and an ABET Program Evaluator (PA). He is a senior member of IEEE and has research interests in distributed power generations, optimization, and engineering education. Dr. Kalaani may be reached at yalkalaani@georgiasouthern.edu.